

Origin of the Resistivity Anisotropy in the Nematic Phase of FeSe

M. A. Tanatar,^{1,2,*} A. E. Böhmer,¹ E. I. Timmons,^{1,2} M. Schütt,³ G. Drachuck,^{1,2}
V. Taufour,¹ S. L. Bud'ko,^{1,2} P. C. Canfield,^{1,2} R. M. Fernandes,³ and R. Prozorov^{1,2,†}

¹*Ames Laboratory, Ames, Iowa 50011, USA*

²*Department of Physics and Astronomy, Iowa State University, Ames, Iowa 50011, USA*

³*School of Physics and Astronomy, University of Minnesota, Minneapolis, Minnesota 55455, USA*

(Dated: 15 November 2015)

The in-plane resistivity anisotropy is studied in strain-detwinned single crystals of FeSe. In contrast to other iron-based superconductors, FeSe does not develop long-range magnetic order below the nematic/structural transition at $T_s \approx 90$ K. This allows for the disentanglement of the contributions to the resistivity anisotropy due to nematic and magnetic orders. Comparing direct transport and elastoresistivity measurements, we extract the intrinsic resistivity anisotropy of strain-free samples. The anisotropy peaks slightly below T_s and decreases to nearly zero on cooling down to the superconducting transition. This behavior is consistent with a scenario in which the in-plane resistivity anisotropy in FeSe is dominated by inelastic scattering by anisotropic spin fluctuations.

PACS numbers: 74.70.Xa, 72.15.-v, 74.25.Ld

Electronic nematicity has emerged as a key concept in iron-based superconductors since the observation of in-plane resistivity anisotropy in stress-detwinned crystals of Co-doped BaFe_2As_2 [1, 2]. The fact that the resistivity anisotropy is much larger than what is expected from the small lattice distortion led to the proposal that the tetragonal-to-orthorhombic transition in the iron pnictides is driven not by phonons, but by an electronic nematic phase. Subsequent experiments revealed an intricate dependence of the resistivity anisotropy on doping (a sign change between electron- and hole-doped materials [2–6]), and disorder [7, 8], sparking hot debates about its microscopic origins (see Refs. [9 and 10] for reviews).

Electronic contributions involved in the in-plane resistivity anisotropy [10] can be separated into the Drude weight and/or of the scattering rate anisotropies. Fermi-surface anisotropies arising, for instance, from the ferro-orbital order triggered at the nematic transition, affect mostly the Drude weight [11–13]. Anisotropic scattering, can be due to elastic processes, such as the development of local magnetic order around an impurity [14, 15], or inelastic processes, such as the scattering of electrons by anisotropic magnetic fluctuations [16, 17] known to exist below T_s [18]. Recent stress-dependent optical reflectivity studies in Co-doped BaFe_2As_2 point to a dominant effect of the Drude weight [19, 20]. However, stripe magnetic order appearing at the magnetic transition severely complicates the analysis. This is because the magnetic state breaks tetragonal symmetry leading to an anisotropic reconstruction of the Fermi surface [7, 21] and to the appearance of “Dirac cones” [22], which may dramatically alter the resistivity anisotropy [23]. Disentangling these contributions is fundamental to reveal the origin of the resistivity anisotropy and, consequently, of the nematic state.

In this context, the stoichiometric FeSe [24] is an ideal system. It is rather clean (residual resistivity ratios as

high as 50 [25]) and its orthorhombic/nematic phase transition at $T_s \approx 90$ K is not accompanied by a long-range magnetic order [26] eliminating effects of Fermi surface folding.

In this Letter we report the resistivity anisotropy measured in strain-detwinned single crystals of FeSe. Upon cooling, the anisotropy $\Delta\rho(T) \equiv \rho_a - \rho_b$ (ρ_a and ρ_b are the resistivities along the orthorhombic a - and b -directions) initially increases, reaching a maximum at about 20 K below T_s , and then nearly vanishes upon further cooling towards the superconducting transition $T_c \approx 8.5$ K. This pronounced non-monotonic behavior is consistent with the scenario in which the main contributor to the resistivity anisotropy is inelastic scattering by magnetic fluctuations rather than the anisotropy of the elastic scattering or of the Fermi surface. To support this conclusion, we performed model calculations of resistivity anisotropy for the scattering of electrons by anisotropic magnetic fluctuations. We find that the anisotropy is well described by the product of two temperature-dependent functions, $\Delta\rho(T) = \Upsilon(T)\phi(T)$. The standard nematic order parameter, $\phi(T)$, increases upon cooling and the scattering function, $\Upsilon(T)$, decreases and vanishes as the temperature approaches zero.

Single crystals of FeSe (~ 1 mm² surface area and 20 to 150 μm thick) were grown using a modified chemical vapor transport as in Ref. 27. Polarized light optical imaging [1, 28] was used to characterize the orthorhombic domain pattern appearing below T_s as shown in Fig. 1. In the orthorhombic phase, the optical birefractance is anisotropic, which permits visualization of domains of different orientations. In addition to direct imaging, we extract the nematic order parameter from the temperature evolution of the color intensity in a small and clean area of the sample (white box in Fig.1(a)), using a decomposition in red, blue and green (RGB) channels [29]. The intensity histograms of the RGB channels

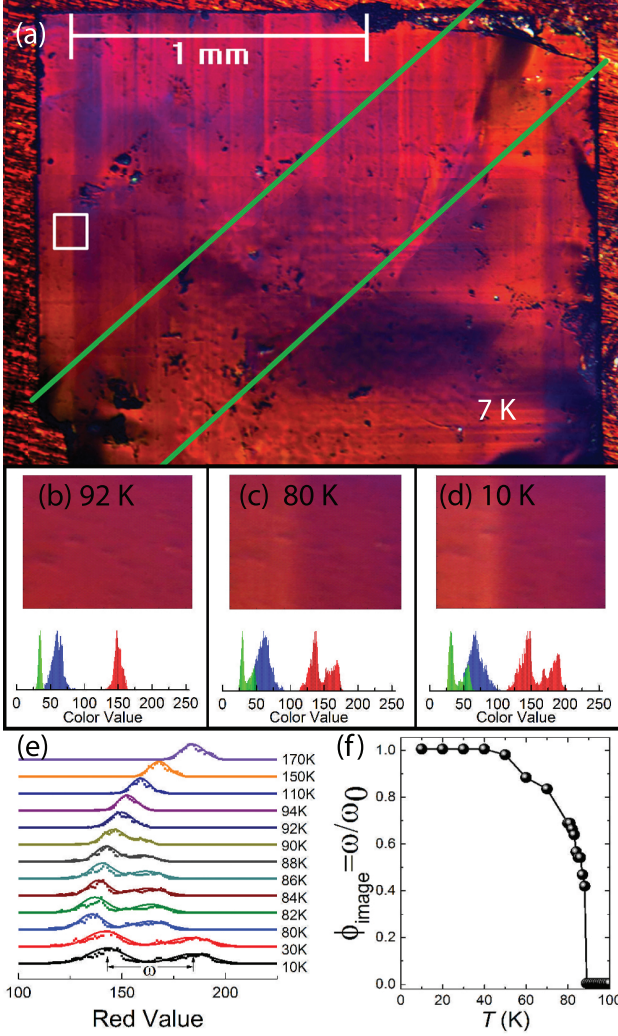


FIG. 1. (color online) (a) Polarized light image of FeSe single crystal at 7 K, revealing orthorhombic domains oriented along tetragonal [100] direction (parallel to the sample sides). For detwinning, the sample is cut along the [110] tetragonal direction as indicated by the green lines. Enlarged are the views of the area indicated by the white box in (a) and corresponding RGB histograms taken at (b) 92 K, (c) 80 K and (d) 10 K. The change below T_s is most pronounced in the red channel (b-d) and temperature evolution of its histograms is shown in panel (e). The peak splitting ω was analyzed using a fit to two gaussians (lines in (e)) and normalized nematic order parameter, $\phi_{\text{image}} \equiv \omega(T)/\omega(T \rightarrow 0)$, is shown in panel (f).

are shown in Figs.1(b), (c), (d). Above T_s the image is of uniform color, manifesting as single peaks in the histograms (panel (b)). Below T_s the domains of different colors lead to peak splitting in the histograms, most pronounced in the red channel (Figs.1(c), (d)). The temperature evolution of the red channel histogram is shown in panel (e). The peak splitting, ω , signaling the breaking of tetragonal symmetry, was determined using a fit to two gaussians and the normalized nematic order param-

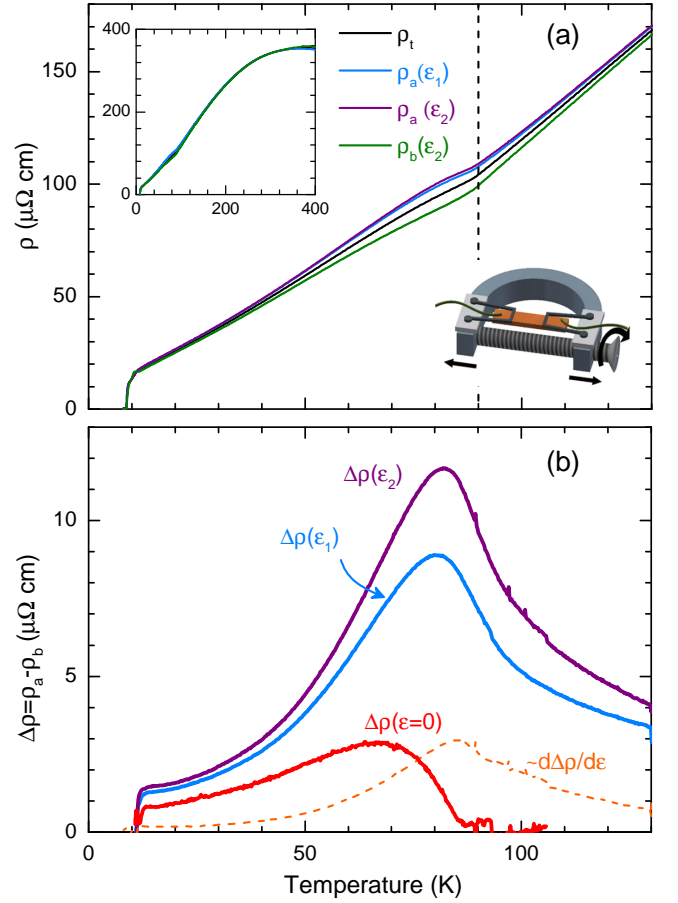


FIG. 2. (color online) (a) Temperature dependent resistivity of FeSe measured in a free-standing state, ρ_t (black curve), and under two values of uniaxial tensile strain, $\epsilon_a = \epsilon_1, \epsilon_2$, representing a fully detwinned state, ρ_a (blue and purple curves). The resistivity along the orthorhombic b direction was calculated as $\rho_b = 2\rho_t - \rho_a$ (green curve). The insets show the whole temperature range and the schematics of the horseshoe detwinning device. (b) Resistivity anisotropy, $\Delta\rho \equiv \rho_a - \rho_b$ for the two values of strain, ϵ_1 and ϵ_2 . Their difference $\Delta\rho(\epsilon_1) - \Delta\rho(\epsilon_2)$ is proportional to the strain-derivative $d\Delta\rho/d\epsilon_a$ (dashed orange line). The latter was used to extract the intrinsic (strain-free) in-plane anisotropy of the resistivity $\Delta\rho(\epsilon_a = 0) \approx \Delta\rho(\epsilon_2) - \frac{d\Delta\rho}{d\epsilon_a} \epsilon_2$ in the orthorhombic phase (red line).

eter, defined as $\phi_{\text{image}}(T) \equiv \omega(T)/\omega(T \rightarrow 0)$, is shown in Fig.1(f).

Samples for mechanical detwinning were cut along the tetragonal [110] direction, which becomes the orthorhombic a or b axis on cooling, as shown schematically by the green lines in Fig. 1(a). Tensile strain was applied to the sample through 50 μm Ag wires also used as potential leads, inset in Fig. 2(a). Wires for current contacts were mounted strain-free. All contacts were In-soldered. Figure 2(a) shows the resistivity of the FeSe sample measured in the strain-free twinned state, ρ_t , and in the detwinned state achieved by application of tensile

strain ε_a of two different magnitudes, $\rho_a(\varepsilon_1)$ and $\rho_a(\varepsilon_2)$. $\varepsilon_a = \varepsilon_1, \varepsilon_2$ is controlled by pulling apart the arms of the horseshoe device. In the strain-free, twinned state ρ_t shows only a small kink at T_s . The sample is split into approximately equal areas of domains of two orientations, so its resistivity is $\rho_t = (\rho_a + \rho_b)/2$. Together with the measurements in detwinned samples, this allows us to extract the resistivity along the orthorhombic b axis, ρ_b , and the in-plane anisotropy, $\Delta\rho$, shown in Fig. 2(b) for two strain values. The anisotropy increases markedly on cooling, evolves smoothly through T_s and peaks below T_s . On further cooling it decreases reaching small values at T_c . Note that $\Delta\rho > 0$, i.e., the resistivity is larger along the a direction, thus having the same sign as that of FeTe [30] and hole-doped BaFe_2As_2 compounds [4], and opposite to electron-doped and isovalently substituted BaFe_2As_2 [1, 2, 31].

The application of strain not only promotes the formation of orthorhombic domains of only one orientation below T_s , but it also induces resistivity anisotropy above and below T_s due to the elastoresistivity of the material. Figure 3(a) shows the elastoresistivity coefficients $2m_{66}$ and $m_{11} - m_{12}$ measured using a piezo-based setup, similar to that described in Refs. [32 and 33]. Samples of approximate dimensions, $1 \times 0.3 \times 0.07 \text{ mm}^3$, were glued to one side of a piezostack, shown in the left inset in Fig. 3(a). The change of sample resistance was measured as a function of anisotropic strain, monitored *in situ* using crossed strain gauges glued to the opposite side of the piezostack. The elastoresistivity coefficient $2m_{66}$ corresponds to the normalized derivative of $\Delta\rho$ with respect to the orthorhombic shear strain $\varepsilon_a - \varepsilon_b$, $2m_{66} = \frac{1}{\rho} \frac{d\Delta\rho}{d(\varepsilon_a - \varepsilon_b)}$ [33]. It clearly diverges on approaching T_s from above (Fig. 3(a)) following almost perfect Curie-Weiss law, $2m_{66} \sim 1/(T - T_0)$ with $T_0 \approx 83 \text{ K}$ (right inset in Fig. 3(a)), in qualitative agreement with previous report [34]. The elastoresistivity mode, $m_{11} - m_{12}$, “orthogonal” to $2m_{66}$, is related to the derivative of the resistivity anisotropy between two diagonals of the orthorhombic unit cell, $[110]_o$ and $[1\bar{1}0]_o$, with respect to the corresponding shear strain, $m_{11} - m_{12} = \frac{1}{\rho} \frac{d(\rho_{[110]_o} - \rho_{[1\bar{1}0]_o})}{d(\varepsilon_{[110]_o} - \varepsilon_{[1\bar{1}0]_o})}$ [33]. This mode does not couple to the nematic order parameter and is, as expected, almost zero above T_s . In the strain-free samples, $\Delta\rho = 0$ is expected for $T > T_s$ and the observed finite resistivity anisotropy is likely a consequence of the applied strain. We therefore compare in Fig. 3(b) the resistivity anisotropy under applied strain ε_2 , given in this case by $\Delta\rho(\varepsilon_2) = \varepsilon_2 \left(\frac{d\Delta\rho}{d\varepsilon_a} \right)$, with the elastoresistivity data. Because $2m_{66} = \frac{1}{\rho_t} \frac{d\Delta\rho}{d(\varepsilon_a - \varepsilon_b)}$ we use the identity, $\frac{d(\varepsilon_a - \varepsilon_b)}{d\varepsilon_a} = 1 + \nu_{\text{FeSe}}$ to transform between strain derivatives. Here, ν_{FeSe} is the Poisson ratio of FeSe calculated from ultrasound data [35]. Clearly, $\Delta\rho(\varepsilon_2)$ and $2m_{66} \rho_t (1 + \nu_{\text{FeSe}}) = \frac{d\Delta\rho}{d\varepsilon_a}$ behave similarly for $T > T_s$, explaining experimentally observed tail of $\Delta\rho$

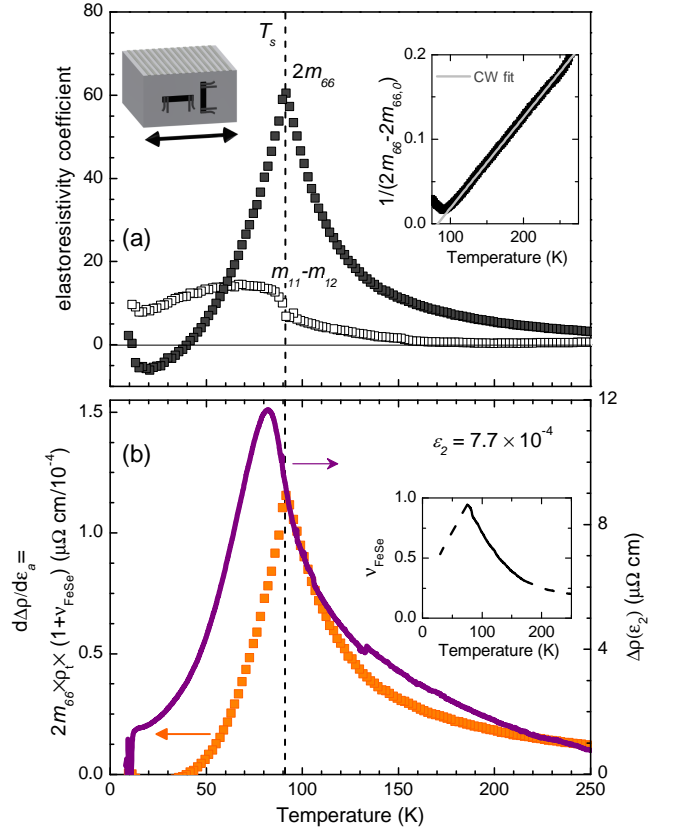


FIG. 3. (color online) (a) Elastoresistivity coefficients $2m_{66}$ and $m_{11} - m_{12}$ of FeSe measured using crossed samples glued to a piezostack, shown schematically in the left inset. The right inset shows the inverse of $m_{66} - m_{66,0}$ demonstrating nearly perfect Curie-Weiss-like behavior, $m_{66} = A/(T - T_0) + m_{66,0}$ with $m_{66,0} = -2.6$ and $T_0 = 83 \text{ K}$. (b) Scaling of $2m_{66} = \frac{1}{\rho_t} \frac{d\Delta\rho}{d(\varepsilon_a - \varepsilon_b)}$ with the resistivity anisotropy, $\Delta\rho(\varepsilon_2)$, measured in detwinned samples. Here, we assume that $\Delta\rho(\varepsilon_2)$ is induced by the applied strain above T_s , so that $\Delta\rho(\varepsilon_2) = \varepsilon_2 \left(\frac{d\Delta\rho}{d\varepsilon_a} \right)$ and use the identity $\frac{d(\varepsilon_a - \varepsilon_b)}{d\varepsilon_a} = 1 + \nu_{\text{FeSe}}$ to transform between the two quantities. The inset shows the Poisson ratio of FeSe ν_{FeSe} determined from the ultrasound data of Ref. [35] (solid line), and extrapolated to 250 K and below T_s (dashed lines).

above T_s . The scaling yields $\varepsilon_2 = 7.7 \times 10^{-4}$ ($\sim 40\%$ of the distortion in the orthorhombic phase) for the external strain applied through the horseshoe device. Below T_s , samples in the elastoresistivity setup are not fully detwinned, so that the domains dominate the measured m_{66} , which prohibits such a comparison.

To determine the effect of strain on the resistivity below T_s , we return to the two resistivity curves at constant strain $\rho_a(\varepsilon_1)$ and $\rho_a(\varepsilon_2)$ in Fig. 2(b) obtained using the horseshoe device, which fully detwinds the samples. In the linear response regime, we can approximate $\frac{d\Delta\rho}{d\varepsilon_a} \approx \frac{\Delta\rho(\varepsilon_2) - \Delta\rho(\varepsilon_1)}{\varepsilon_2 - \varepsilon_1}$. The derivative is used to extract the intrinsic resistivity anisotropy between the a and b directions of a single-domain sample in the absence of

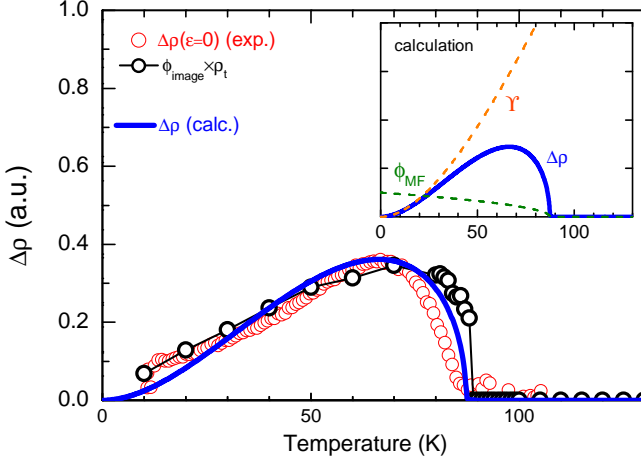


FIG. 4. (color online) Experimental temperature-dependent resistivity anisotropy in the zero-strain limit (from Fig. 2 (b), red symbols), $\Delta\rho(T)$, compared to the product of the temperature-dependent experimentally determined order parameter ϕ_{image} of Fig. 1(g) and the isotropic resistivity ρ_t of Fig. 2(a) (black circles). The blue line shows the results of a model calculation where $\Delta\rho$ is determined by the product of a mean-field-type order nematic parameter $\phi(T)$ and a temperature dependent function $\Upsilon(T)$ resulting from inelastic scattering promoted by spin fluctuations (see inset).

external strain, $\Delta\rho(\varepsilon = 0) \approx \Delta\rho(\varepsilon_2) - \frac{\Delta\rho(\varepsilon_2) - \Delta\rho(\varepsilon_1)}{\varepsilon_2 - \varepsilon_1} \varepsilon_2$. The constant value of $\frac{\varepsilon_2}{\varepsilon_2 - \varepsilon_1} \approx 3.7$ is fixed by enforcing $\Delta\rho(\varepsilon = 0) = 0$ in the tetragonal state. The resulting $\Delta\rho(\varepsilon = 0)$ (red line in Fig. 2(b)) clearly displays a broad maximum 20 K below T_s .

The previous comparison between m_{66} and $\Delta\rho$ reveals that, above T_s , the resistivity anisotropy is proportional to the strain, and therefore to the nematic order parameter ϕ . A similar behavior was experimentally observed in the iron pnictides [29]. This relationship indeed is more general: because $\Delta\rho$ and ϕ break the same symmetry, they are generally proportional to each other, i.e. $\Delta\rho = \Upsilon\phi$, where Υ is the proportionality factor [32, 36]. It is clear from Fig. 1 that ϕ displays a standard order-parameter behavior, monotonically increasing upon cooling. In contrast, the resistivity anisotropy, $\Delta\rho$, shows a pronounced peak below T_s and decreases to nearly zero at $T \rightarrow 0$. This behavior must therefore arise from the temperature-dependence of the proportionality factor, Υ , which should also vanish as $T \rightarrow 0$, since ϕ remains finite and large at $T \rightarrow 0$. Among the possible microscopic contributions to $\Delta\rho$ affecting Υ – anisotropies of Fermi surface, elastic and inelastic scattering rates, only the latter one naturally leads to the observed behavior. Phenomenologically, this is nicely illustrated by using ϕ_{image} of Fig. 1 as a proxy of ϕ , and the resistivity of the twinned sample, $\rho_t(T)$, as a proxy of Υ . The latter relies on the assumption that the inelastic scattering also dominates the isotropic transport properties. Indeed, the product

$\phi_{\text{image}}(T)\rho_t(T)$, shown by the black symbols in Fig. 4, captures much of the temperature dependence of $\Delta\rho(T)$.

In order to develop a microscopic scenario for this behavior, we consider the three-band model of Ref. [16], in which electrons are scattered by magnetic fluctuations. This model contains one circular hole pocket at the center of the Brillouin zone and two electron pockets centered at momenta $(\pi, 0)$ and $(0, \pi)$. Below T_s , the onset of nematic order leads to stronger fluctuations at the ordering vector $(\pi, 0)$ than at $(0, \pi)$, a behavior observed experimentally by the neutron scattering [18]. Depending on the relative positions of the hot spots – points of the hole and electron pockets connected by the ordering vectors – one finds $\rho_a > \rho_b$ or $\rho_b > \rho_a$ (see also Ref. [17]). Indeed, the change in the positions of the hot spots from hole-doping to electron-doping was argued in Ref. [4] as a possible reason for the sign change of $\Delta\rho$. Using the formalism developed in Ref. [16], we perform an expansion of the resistivity anisotropy, finding $\Delta\rho = \Upsilon\phi$. Here, we assume $\phi(T)$ to display a mean-field like behavior $\phi(T) = \phi_0\sqrt{1 - T/T_s}$. The proportionality constant Υ , arising from the scattering of electrons by magnetic excitations, depends on the magnetic correlation length, ξ , and on the Landau damping of the magnetic fluctuations, Γ . In particular, we find $\Upsilon = \Upsilon_0 T (1 + 3\Gamma\xi^{-2}/2\pi T)^{-1}$, where Υ_0 is a constant that depends on the geometry of the Fermi surface and on the residual resistivity. This leads to $\Upsilon(T \rightarrow 0) \sim T^2$, and therefore, the different temperature dependencies of $\phi(T)$ and $\Upsilon(T)$ gives rise to a maximum in $\Delta\rho$ below T_s . This behavior is illustrated in Fig. 4, where we plot the calculated $\Delta\rho$ for $\xi = 3a$ and $\Gamma = 150$ meV (the product $\phi_0\Upsilon_0$ is treated as a fitting parameter to the data). Note that ξ was assumed to be small and temperature-independent above T_s , in agreement with the NMR data [37, 38]. Below T_s , the onset of nematic order renormalizes ξ and leads to its enhancement [39], as observed in the same NMR data. The good agreement between the calculated and the measured $\Delta\rho$ suggests that the inelastic scattering by anisotropic magnetic fluctuations can explain the experimentally observed non-monotonic temperature-dependence of the in-plane resistivity anisotropy.

In conclusion, the comparison of direct transport and elastoresistivity measurements in FeSe was used to extract the intrinsic in-plane resistivity anisotropy of strain-free samples. Strong non-monotonic temperature dependence, displaying a maximum below T_s and becoming very small as $T \rightarrow 0$ limit was observed. This behavior is explained by anisotropic inelastic scattering as a main contribution to $\Delta\rho$, shedding new light on the origin of nematicity in iron-based superconductors.

The experimental work was supported by the U.S. Department of Energy (DOE), Office of Basic Energy Sciences, Division of Materials Sciences and Engineering. The experimental research was performed at Ames Laboratory, which is operated for the U.S. DOE by

Iowa State University under Contract No. DE-AC02-07CH11358. M. S. acknowledges the support from the Humboldt Foundation. R. M. F. is supported by the U.S. Department of Energy, Office of Science, Basic Energy Sciences, under Award No. DE-SC0012336. G. D. was funded by the Gordon and Betty Moore Foundations EPiQS Initiative through Grant GBMF4411.

* corresponding author: tanatar@ameslab.gov

† corresponding author: prozorov@ameslab.gov

- [1] M. A. Tanatar, E. C. Blomberg, A. Kreyssig, M. G. Kim, N. Ni, A. Thaler, S. L. Bud'ko, P. C. Canfield, A. I. Goldman, I. I. Mazin and R. Prozorov, *Phys. Rev. B* **81**, 184508 (2010).
- [2] J.-H. Chu, J. G. Analytis, K. De Greve, P. L. McMahon, Z. Islam, Y. Yamamoto, and I. R. Fisher, *Science* **329**, 824 (2010).
- [3] J. J. Ying, X. F. Wang, T. Wu, Z. J. Xiang, R. H. Liu, Y. J. Yan, A. F. Wang, M. Zhang, G. J. Ye, P. Cheng, J. P. Hu, and X. H. Chen, *Phys. Rev. Lett.* **107**, 067001 (2011).
- [4] E. C. Blomberg, M. A. Tanatar, R. M. Fernandes, I. I. Mazin, Bing Shen, Hai-Hu Wen, M. D. Johannes, J. Schmalian, and R. Prozorov, *Nature Comm.* **4**, 1914 (2013).
- [5] J. Q. Ma, X. G. Luo, P. Cheng, N. Zhu, D. Y. Liu, F. Chen, J. J. Ying, A. F. Wang, X. F. Lu, B. Lei, and X. H. Chen *Phys. Rev. B* **89**, 174512 (2014)
- [6] Tatsuya Kobayashi, Kiyohisa Tanaka, Shigeki Miyasaka, Setsuko Tajima, *J. Phys. Soc. Jpn.* **84**, 094707 (2015).
- [7] Taichi Terashima, Nobuyuki Kurita, Megumi Tomita, Kunihiro Kihou, Chul-Ho Lee, Yasuhide Tomioka, Toshimitsu Ito, Akira Iyo, Hiroshi Eisaki, Tian Liang, Masamichi Nakajima, Shigeyuki Ishida, Shin-ichi Uchida, Hisatomo Harima, and Shinya Uji, *Phys. Rev. Lett.* **107**, 176402 (2011).
- [8] Hsueh-Hui Kuo and Ian R. Fisher, *Phys. Rev. Lett.* **112**, 227001 (2014).
- [9] I. R. Fisher, L. Degiorgi, and Z.X. Shen, *Rep. Progr. Phys.* **74**, 124506 (2011).
- [10] R. M. Fernandes, A. V. Chubukov, J. Schmalian, *Nature Phys.* **10**, 97 (2014).
- [11] C.-C. Chen, J. Maciejko, A. P. Sorini, B. Moritz, R. R. P. Singh, and T. P. Devereaux, *Phys. Rev. B* **82**, 100504 (2010).
- [12] Weicheng Lv and Philip Phillips, *Phys. Rev. B* **84**, 174512 (2011).
- [13] S. Liang, G. Alvarez, C. Sen, A. Moreo, and E. Dagotto, *Phys. Rev. Lett.* **109**, 047001 (2012).
- [14] M. P. Allan, T.-M. Chuang, F. Massee, Yang Xie, Ni Ni, S. L. Bud'ko, G. S. Boebinger, Q. Wang, D. S. Dessau, P. C. Canfield, M. S. Golden, and J. C. Davis, *Nature Phys.* **9**, 220 (2013).
- [15] Maria N. Gastiasoro, I. Paul, Y. Wang, P. J. Hirschfeld, Brian M. Andersen, *Phys. Rev. Lett.* **113**, 127001 (2014).
- [16] Rafael M. Fernandes, Elihu Abrahams, and Jörg Schmalian, *Phys. Rev. Lett.* **107**, 217002 (2011).
- [17] Maxim Breitzkreiz, Philip M. R. Brydon, and Carsten Timm, *Phys. Rev. B* **90**, 121104(R) (2014).
- [18] Xingye Lu, J. T. Park, Rui Zhang, Huiqian Luo, Andriy H. Nevidomskyy, Qimiao Si, and Pengcheng Dai, *Science* **345**, 657 (2014).
- [19] C. Mirri, A. Dusza, S. Bastelberger, J.-H. Chu, H.-H. Kuo, I. R. Fisher, and L. Degiorgi, *Phys. Rev. B* **90**, 155125 (2014).
- [20] C. Mirri, A. Dusza, S. Bastelberger, M. Chinotti, L. Degiorgi, J.-H. Chu, H.-H. Kuo, and I. R. Fisher, *Phys. Rev. Lett.* **115**, 107001 (2015).
- [21] B. Valenzuela, E. Bascones, and M. J. Calderon, *Phys. Rev. Lett.* **105**, 207202 (2010).
- [22] Khuong K. Huynh, Yoichi Tanabe, and Katsumi Tanigaki, *Phys. Rev. Lett.* **106**, 217004 (2011).
- [23] Hsueh-Hui Kuo, Jiun-Haw Chu, Scott C. Riggs, Leo Yu, Peter L. McMahon, Kristiaan De Greve, Yoshihisa Yamamoto, James G. Analytis, and Ian R. Fisher, *Phys. Rev. B* **84**, 054540 (2011).
- [24] Fong-Chi Hsu, Jiu-Yong Luo, Kuo-Wei Yeh, Ta-Kun Chen, Tzu-Wen Huang, Phillip M. Wu, Yong-Chi Lee, Yi-Lin Huang, Yan-Yi Chu, Der-Chung Yan, Maw-Kuen Wu, *Proc Natl. Acad. Sci. U S A.* **105**, 14262 (2008).
- [25] Shigeru Kasahara, Tatsuya Watashige, Tetsuo Hanaguri, Yuhki Kohsaka, Takuya Yamashita, Yusuke Shimoyama, Yuta Mizukami, Ryota Endo, Hiroaki Ikeda, Kazushi Aoyama, Taichi Terashima, Shinya Uji, Thomas Wolf, Hilbert von Löhneysen, Takasada Shibauchi, and Yuji Matsuda, *Proc. Nat. Acad. Sci.* **111** 16309 (2014).
- [26] T. M. McQueen, A. J. Williams, P. W. Stephens, J. Tao, Y. Zhu, V. Ksenofontov, F. Casper, C. Felser, and R. J. Cava, *Phys. Rev. Lett.* **103**, 057002 (2009).
- [27] A. E. Böhmer, F. Hardy, F. Eilers, D. Ernst, P. Adelmann, P. Schweiss, T. Wolf, C. Meingast, *Phys. Rev. B* **87**, 180505(R) (2013).
- [28] M. A. Tanatar, A. Kreyssig, S. Nandi, N. Ni, S. L. Bud'ko, P. C. Canfield, A. I. Goldman, and R. Prozorov, *Phys. Rev. B* **79**, 180508 (R) (2009).
- [29] E. C. Blomberg, A. Kreyssig, M. A. Tanatar, R. M. Fernandes, M. G. Kim, A. Thaler, J. Schmalian, S. L. Bud'ko, P. C. Canfield, A. I. Goldman, and R. Prozorov, *Phys. Rev. B* **85**, 144509 (2012).
- [30] Juan Jiang, C. He, Y. Zhang, M. Xu, Q. Q. Ge, Z. R. Ye, F. Chen, B. P. Xie, and D. L. Feng, *Phys. Rev. B* **88**, 115130 (2013).
- [31] H.-H. Kuo, James G. Analytis, J.-H. Chu, R. M. Fernandes, J. Schmalian, and I. R. Fisher, *Phys. Rev. B* **86**, 134507 (2012).
- [32] J.-H. Chu, H.-H. Kuo, J. G. Analytis, I. R. Fisher, *Science* **337**, 710 (2012).
- [33] Hsueh-Hui Kuo, Maxwell C. Shapiro, Scott C. Riggs, and Ian R. Fisher, *Phys. Rev. B* **88**, 085113 (2013).
- [34] M. D. Watson, T. K. Kim, A. A. Haghighirad, N. R. Davies, A. McCollam, A. Narayanan, S. F. Blake, Y. L. Chen, S. Ghannadzadeh, A. J. Schofield, M. Hoesch, C. Meingast, T. Wolf, and A. I. Coldea, *Phys. Rev. B* **91**, 155106 (2015).
- [35] G. A. Zvyagina, T. N. Gaydamak, K. R. Zhekov, I. V. Bilich, V. D. Fil, D. A. Chareev, and A. N. Vasiliev, *Europhys. Lett.* **101**, 56005 (2013).
- [36] Michael Schütt and Rafael M. Fernandes, *Phys. Rev. Lett.* **115**, 027005 (2015).
- [37] A. E. Böhmer, T. Arai, F. Hardy, T. Hattori, T. Iye, T. Wolf, H. v. Löhneysen, K. Ishida, and C. Meingast, *Phys. Rev. Lett.* **114**, 027001 (2015).

- [38] S. H. Baek, D. V. Efremov, J. M. Ok, J. S. Kim, Jeroen van den Brink, and B. Büchner, *Nature Materials* **14**, 210 (2015).
- [39] Qiang Zhang, Rafael M. Fernandes, Jagat Lamsal, Jiaqiang Yan, Songxue Chi, Gregory S. Tucker, Daniel K. Pratt, Jeffrey W. Lynn, R. W. McCallum, Paul C. Canfield, Thomas A. Lograsso, Alan I. Goldman, David Vaknin, and Robert J. McQueeney, *Phys. Rev. Lett.* **114**, 057001 (2015).